Separation and Purification Technology 379 (2025) 135124

Contents lists available at ScienceDirect

Separation and Purification Technology

journal homepage: www.elsevier.com/locate/seppur

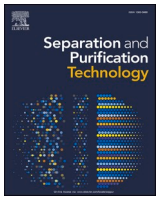

Fe − Modified and N − Doped sludge biochar for BPA Removal: PI-Activated Nonradical oxidation Coupled with synergistic adsorption

Haochun Zang [a], Yihan Huang [a], Tong Hao [a], Shuhu Xiao [a], Juanjuan Zhang [a], Haibo Li [c], Bingfei Yan [a,b,*]

[a] State Key Laboratory of Environmental Criteria and Risk Assessment, Chinese Research Academy of Environmental Sciences, Beijing 100012, China
[b] College of Water Sciences, Beijing Normal University, Beijing 100875, China
[c] School of Environmental and Municipal Engineering, Tianjin Key Laboratory of Aquatic Science and Technology, Tianjin Chengjian University, Tianjin 300384, China

ARTICLE INFO

Keywords:
Fe@N−SBC
Periodate
Bisphenol A
Advanced oxidation technology
Synergistic adsorption and catalysis

ABSTRACT

Persistent organic pollutants (POPs) such as bisphenol A (BPA) pose serious environmental and health threats due to their stability and resistance to conventional treatments. To address this challenge, developing catalysts that enable simultaneous adsorption and catalytic degradation represents a reliable strategy. In this study, a Fe and N co-doped biochar (Fe@N − SBC) with dual adsorption and catalytic capabilities was synthesized via a simple pyrolysis method using sewage sludge as a precursor, offering a sustainable route for waste sludge into high-value catalysts and aiming for the efficient removal of Bisphenol A (BPA). The material achieved rapid BPA removal (96.1 % within 60 min) through a synergistic adsorption–activation mechanism. Mechanistic analyses confirmed that π–π electron donor–acceptor (EDA) interactions, electrostatic interactions, hydrogen bonding and surface complexation governed adsorption, while Fe(II)/Fe(III) redox cycling, as well as the presence of Fe–Nx, pyridinic N and C=O functional groups, played a crucial role in PI activation. Both radical (RIS and $^{\bullet}OH$) and non-radical ($^1O_2$) species were identified as the main contributors. Theoretical analyses revealed that the adsorption process confined BPA near Fe@N–SBC active sites, shortening the reaction pathway between reactive species and the pollutant. Meanwhile, Fe@N − SBC prolonged the I − O bond of PI and enhanced interfacial electron transfer, thus improving the generation of reactive species through both radical and non-radical pathways. This study not only provides new mechanistic insights into PI activation but also highlights the potential of waste-derived biochar as sustainable catalysts for wastewater treatment.

1. Introduction

Bisphenol A (BPA) is a typical endocrine-disrupting compound (EDC), which is widely detected in various aquatic environments due to its extensive use in polycarbonate plastics and epoxy resins [1,2]. Reports have shown that BPA concentrations in surface waters have reached 50–80 μ g/L in several countries, while levels exceeding 200 μg/L have been reported in groundwater [3]. BPA has been detected in human blood and other body fluids, with concentrations exceeding thresholds known to trigger adverse biological effects [4]. Wastewater from certain industrial facilities, particularly paper manufacturing plants, has been identified as a major source of BPA, with concentrations far exceeding typical environmental levels and exhibiting strong resistance to conventional treatment methods. Given its persistence, bioaccumulation potential, and endocrine-disrupting effects, the development of advanced catalytic materials for effective BPA removal is necessary. Various treatment approaches–including physical adsorption [5], biological treatment [6] and chemical oxidation [7] have been explored for BPA removal. However, these methods often face limitations such as low efficiency, high cost and the generation of secondary pollutants [8].

Advanced Oxidation Processes (AOPs) have attracted significant attention as effective technologies for the degradation of toxic and organic pollutants, owing to their high mineralization efficiency, mild reaction conditions and operational simplicity [9]. Among various AOPs, periodate (PI) − based systems have emerged as a promising method for the degradation of BPA [10]. PI is a solid oxidant with a high oxidation potential (+1.60 V) and exhibits good stability, making it convenient for storage and transport [11], thereby minimizing handling risks during application. It's noting that the I − O bond length in PI (1.78

* Corresponding author at: Chinese Research Academy of Environmental Sciences, Beijing, 100012, China.
E-mail address: ybf201506@163.com (B. Yan).

https://doi.org/10.1016/j.seppur.2025.135124
Received 13 August 2025; Received in revised form 1 September 2025; Accepted 8 September 2025
Available online 9 September 2025

Å) is longer than the O − O bond lengths in PMS (1.45 Å), PDS (1.49 Å), and H_2O_2 (1.44 Å), indicating that the I − O bond in PI is more easily cleaved upon activation to form reactive species [12]. It has been demonstrated that PI can be effectively activated to produce highly oxidizing reactive oxygen/iodine species (ROS/RIS) under specific conditions such as light [13], ultrasound [14], alkali [15], transition metals [16] and carbon materials [17]. Additionally, non-radical pathways, including singlet oxygen ($^1O_2$), high-valent metal species and electron transfer, also occurred in the PI activation system [18]. Therefore, the search for low-cost, easily recoverable and environmentally friendly PI activators remains a central challenge.

The increasing volume of sewage sludge generated by urban wastewater treatment plants poses a significant environmental challenge, primarily due to its potential for secondary pollution and the high disposal costs associated with it. Traditional disposal methods, such as landfilling and incineration, not only exacerbate environmental pollution but also fail to exploit the resource potential of sewage sludge. In recent years, the pyrolysis of sewage sludge into biochar has emerged as a promising approach for both sludge reduction and resource recovery. Biochar, with its high surface area, porous structure and abundance of functional groups, has been widely used as an adsorbent and catalyst. Studies demonstrated that biochar can activate periodate (PI), and that its catalytic performance and selectivity toward organic contaminants can be modulated by the pyrolysis temperature. In addition, studies have shown that co − doping of transition metals and nitrogen (N) can alter the electron structure of carbon materials, which enhances the electron − donating capability and facilitates the non − radical mechanism for oxidizing organic contaminants [19]. Both radical and non − radical pathways of PI activation are attributed to the facilitation provided by Fe and N co − doped carbon materials [20]. The adsorption mechanisms of biochar for organic pollutants mainly include hydrogen bonding, electrostatic interactions, π-π interactions and surface complexation [21]. For instance, there have been studies that synthesized a novel Fe–Mg co-modified water hyacinth-based biochar using a co-modification process, which exhibited an adsorption capacity 15.34 times greater than that of unmodified biochar for the removal of imidacloprid from water. However, relying solely on adsorption raises concerns regarding secondary pollution and the difficulty of material regeneration [22]. The introduction of PI significantly enhances the degradation efficiency by generating reactive species through catalytic activation. Compared with free pollutants in water, organic molecules adsorbed on the catalyst surface have a shorter diffusion path to the active sites, facilitating more effective degradation. However, most existing studies focus either on adsorption or on catalytic degradation, overlooking their possible synergy. In addition, the mechanistic understanding of how adsorption influences catalytic PI activation remains limited, such as through confining pollutants at active sites to shorten the reaction pathway and alter the electronic structure of PI (prolonging the I − O bond) to enhance interfacial electron transfer. Additionally, the synthesis of co − doped carbon materials often involves high costs and involves complex processes. Therefore, it is essential to utilize waste resources such as sewage sludge as raw materials to develop low-cost carbon materials doped with Fe and N, evaluating their adsorption performance and PI activation efficiency.

In this study, Fe and N co − doped sludge − based biochar (Fe@N − SBC) was synthesized from sewage sludge through a simple one − step pyrolysis process. The main objectives were (1) to evaluate the adsorption and catalytic performance of Fe@N-SBC through the removal efficiency of BPA; (2) to investigate the degradation kinetics and the effects of key reaction parameters; (3) to identify the active sites of Fe@N − SBC and the RIS/ROS involved in the Fe@N − SBC/PI system. and (4) to elucidate the adsorption and degradation mechanisms of BPA in the Fe@N − SBC/PI system.

2. Materials and methods

2.1. Reagents and catalyst preparation

All reagents are shown in Text S1. Fe@N-SBC was prepared using sewage sludge as a precursor. Specifically, 50 g of dewatered sludge was mixed with $FeSO_4{\cdot}7H_2O$ and NH_4Cl at different Fe/N mass ratios, including 2:1 (3.0 g $FeSO_4{\cdot}7H_2O$ and 1.5 g NH_4Cl), 1:1 (1.5 g $FeSO_4{\cdot}7H_2O$ and 1.5 g NH_4Cl), and 1:2 (1.5 g $FeSO_4{\cdot}7H_2O$ and 3.0 g NH_4Cl) in 100 mL of deionized (DI) water. The mixture was stirred for 12 h to ensure homogeneity, then dried at 105 °C overnight. The dried solid was ground and sieved (100 mesh, <0.074 mm), then pyrolyzed in a tubular furnace at 550 − 950 °C for 2 h under N_2 (200 mL min^{-1}) with a heating rate of 10 °C min^{-1}. The obtained biochar was washed with DI water and ethanol, then dried at 60 °C to yield Fe@N − SBC. Control samples (SBC, N − SBC, Fe − SBC) were synthesized by omitting $FeSO_4{\cdot}7H_2O$, NH_4Cl, or both.

2.2. Catalytic degradation experiments

Unless otherwise stated, all degradation experiments were conducted in 100 mL beakers at 25 ± 2°C. BPA stock solution (100 mg L^{-1}) was diluted to desired concentrations using DI water. The catalyst dosage was 0.40 g L^{-1}, and the solution was stirred at 350 rpm. After 30 min of adsorption, 0.5 mM PI was added to initiate the catalytic reaction. At specified intervals, 1 mL samples were taken, filtered (0.22 μm PTFE), and quenched with 100 μM $Na_2S_2O_3$ (0.1 M). Each experimental condition was performed three times, and the values reported represent the mean results with corresponding standard deviations shown as error bars. Other experimental procedures are shown in Text S2. Materials Characterization methods were shown in Text S3.

2.3. Analytical methods

The concentrations of BPA, 2-Iodophenol (2-IP), 4-Iodophenol (4-IP) and iodine-containing anions (IO_4^-, IO_3^- and I^-) and iodinated byproducts (HOI) were determined using high-performance liquid chromatography (HPLC, Agilent 1260) equipped with a C18 reverse-phase column and UV detector. I_2 and I_3^- formation was assessed via a starch-based colorimetric method. Degradation intermediates of BPA were identified using ultra-high-performance liquid chromatography-mass spectrometry (UPLC-MS), while their ecological toxicity was predicted using the Toxicity Estimation Software Tool (T.E.S.T.). Reactive oxygen species (ROS), including $^{\bullet}OH$, $O_2^{\bullet-}$ and $^1O_2$, were detected by electron paramagnetic resonance (EPR, Bruker A300) using DMPO and TEMP as spin-trapping agents. Electrochemical properties of the catalyst were evaluated with a CHI 760E workstation under a three-electrode system. Additionally, total organic carbon (TOC) analysis and pH measurements were conducted to assess mineralization efficiency and reaction conditions. Detailed experimental procedures and instrumental parameters are provided in Text S4 and Table S1.

2.4. Theoretical calculations

Density functional theory (DFT) calculations were performed using both Gaussian 16 and VASP packages, with geometry optimizations and energy calculations carried out under detailed settings as described in Text S5.

3. Results and discussion

3.1. Characterization of the catalysts

The morphology, structural characteristics and elemental composition of Fe@N − SBC were comprehensively analyzed using scanning electron microscope (SEM) and energy-dispersive X-ray spectrometer

(EDS) mapping to investigate its surface features and elemental distribution. Fe@N − SBC exhibited a rough and uneven porous structure, with irregular sheets and lumpy structures dispersed on the carbon matrix surface (Fig. 1a-b), which were identified as iron oxides. EDS mapping confirmed the uniform distribution of C, N, O and Fe elements throughout the Fe@N − SBC (Fig. 1c-f). In contrast, the surface of SBC (Fig. 1 g-h) appeared more compact and smoother. Although N and Fe elements were also detected in the EDS mapping of SBC, their contents were significantly lower than those in Fe@N − SBC, indicating that the Fe and N in the catalyst mainly originated from the added $FeSO_4{\cdot}7H_2O$ and NH_4Cl (Fig. 1i-l and Table S2-3).

According to the IUPAC classification, the N_2 adsorption–desorption isotherms of the Fe@N − SBC and SBC exhibited typical IV isotherms, indicating that their pore structures are predominantly mesopores (Fig. 1m and Fig. S1) [23]. As shown in Table S4, the specific surface area of Fe@N-SBC-850 (118.04 $m^2\ g^{-1}$) was slightly lower than that of SBC (121.80 $m^2\ g^{-1}$). This phenomenon might be the consumption of carbon material during Fe loading, which reduces the specific surface area [24]. The pore size distribution curves indicated that Fe@N − SBC had a higher pore distribution and a larger average pore diameter (7.03 nm) compared to SBC (5.79 nm). A high specific surface area combined with an abundant pore structure facilitates the adsorption of PI and BPA molecules, enhances the utilization of active sites and accelerates mass transfer, thereby improving the overall catalytic performance.

XRD was conducted to analyze the crystallographic structures of the different biochar − derived catalysts. As shown in Fig. 1n, all derived materials exhibit characteristic diffraction peaks at 26.71° and 44.29°, corresponding to the (0 0 2) and (1 0 1) planes of graphitic carbon (PDF#99-0057) after pyrolysis [25]. Notably, the additional diffraction peaks at 16.55° (1 0 0), 28.02° (1 1 0), 33.80° (2 0 0), 40.91° (0 1 1), 42.95° (1 2 0) and 47.38° (1 1 − 1) were observed, indicating the generation of C_3N_4 (PDF#87-1523) due to N doping [26]. Moreover, the diffraction peaks at 20.86°, 30.02°, 33.82°, 43.60°, 52.98°, 54.18° were assigned to (1 0 5), (0 0 12), (1 1 6), (2 0 10), (3 0 0), and (2 0 16) crystal planes of Fe_2O_3 (PDF#40-1139) [27]. Extra reflection peaks at 35.33° (3 1 1), 43.60° (4 0 0), 47.38° (3 3 1), 52.98° (4 2 2), 70.92° (6 2 0) and 73.92° (5 3 3) corresponding to Fe_3O_4 were observed (PDF#72-2303), suggesting that the Fe in Fe@N − SBC were transformed into Fe_2O_3 and Fe_3O_4 during pyrolysis, which was consistent with previous findings [28,29]. It was observed that the intensity of the graphitic carbon peaks in SBC was stronger than that in Fe@N − SBC, indicating that the co − doping of Fe and N decreased the graphitization of the biochar.

Raman spectra results (Fig. 1O) further confirmed this observation. The Fe@N − SBC (1.21) sample exhibited a higher intensity ratio of the D and G bands (I_D/I_G) compared to SBC (1.10), indicating a greater defect density and lower graphitization degree [30]. The higher I_D/I_G value of Fe@N − SBC indicated that its defect density and graphitization degree were high, which may enhance catalytic performance [31]. The I_D/I_G decreased for used Fe@N − SBC (1.10) after the reaction, implying a potential decline in catalytic performance.

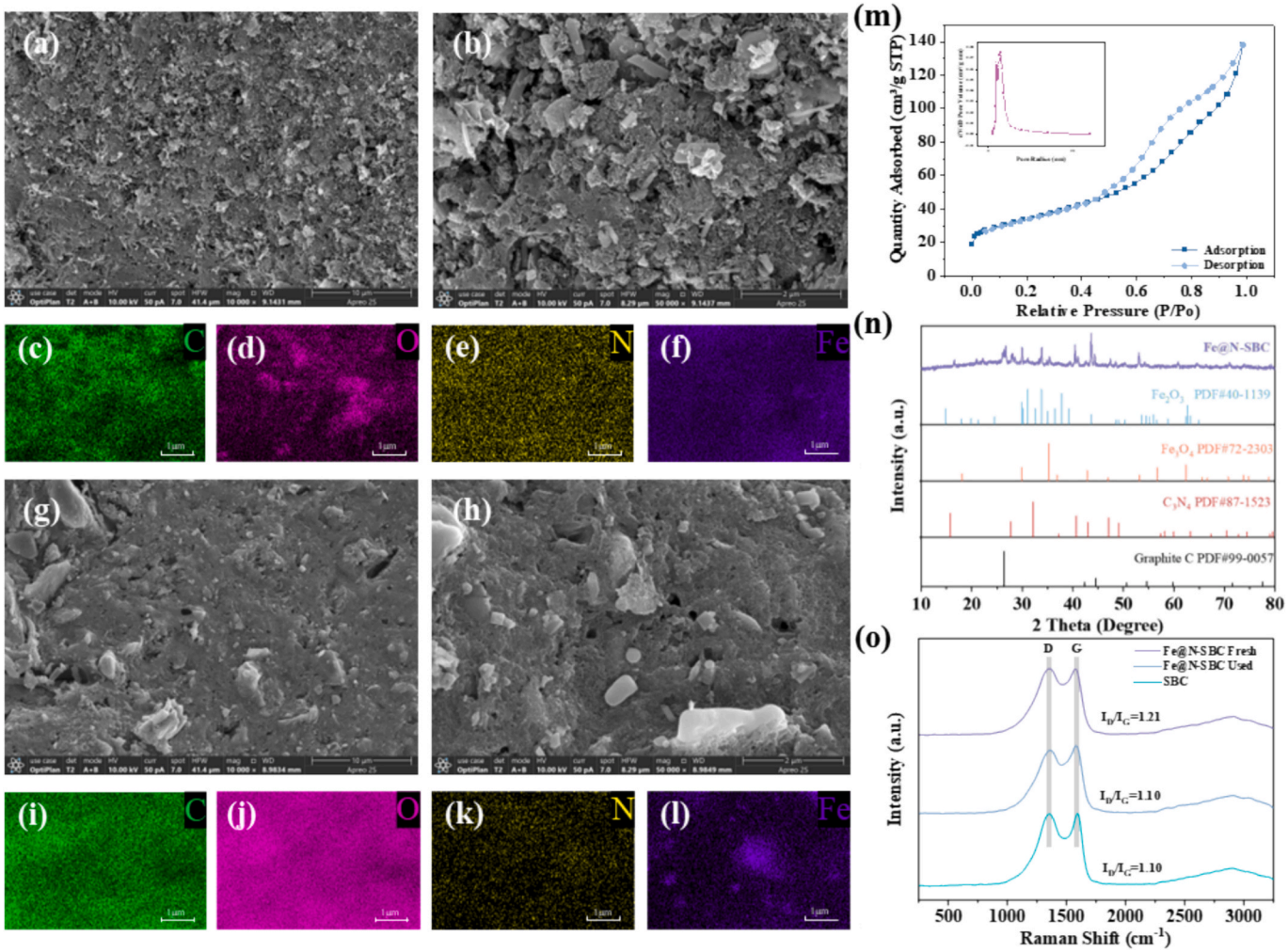

Fig. 1. (a-b) SEM micrographs of Fe@N − SBC, (c-f) EDS-mapping of Fe@N − SBC, (g-h) SEM micrographs of Fe@N − SBC, (i-l) EDS-mapping of Fe@N − SBC, (m) N_2 adsorption–desorption isotherms of Fe@N − SBC. The inset: pore size distribution, (n) XRD pattern of Fe@N − SBC, (o) Raman spectra of SBC, fresh Fe@N − SBC and used Fe@N − SBC.

FTIR spectroscopies were performed to detect surface functional groups of SBC, fresh Fe@N − SBC and used Fe@N − SBC (Fig. 2a). All samples exhibited broad absorption peaks at 3365 cm^{-1}, corresponding to the –OH group [32]. Notably, the − OH stretching vibration in used Fe@N − SBC was suppressed, which may indicate the formation of hydrogen bonds between the − OH groups on BPA and the hydroxyl groups on the carbon material surface (discussed in Section 3.4) [33]. Furthermore, the peak at 1574 cm^{-1} was attributed to C=C, while the signal peak at 1106 cm^{-1} corresponded to C − O − C/C=O [34–36]. In Fe@N − SBC, two prominent peaks at 912 cm^{-1} and 568 cm^{-1} were assigned to C − N and Fe − O vibrations [37]. This confirms the successful preparation of the Fe@N − SBC catalyst. It is worth noting that the weak signal peak at 416 cm^{-1} corresponds to Fe − N in Fe@N − SBC [38]. However, this peak became very weak in used Fe@N − SBC, indicating that Fe − N might be a potential site of the activated PI.

Fig. 2b shows the XPS full-scan spectrum of Fe@N − SBC, revealing the surface elemental composition and chemical states. Characteristic peaks corresponding to C 1 s, O 1 s, N 1 s and Fe 2p were observed. The relative elemental contents of C, N, O and Fe in Fe@N − SBC were 46.51 %, 3.69 %, 48.54 % and 1.25 %, respectively (Table S5). Notably, no significant changes in elemental types or contents were observed before and after the degradation reaction, indicating the structural stability of Fe@N − SBC (Table S6). Fig. 2c-f show the high − resolution spectra of C 1 s, N 1 s, O 1 s and Fe 2p. Typical C 1 s XPS spectrum (Fig. 2c) of Fe@N − SBC exhibited three peaks at 284.80 eV, 285.79 eV and 288.70 eV, corresponding to C–C/C=C, C–N/C–O and C=O, respectively [39–41]. The dominant peak at 284.80 eV corresponds to sp^2 carbon, indicating that graphite C is the main component on the surface of Fe@N − SBC. The high-resolution O 1 s spectra (Fig. 2d) were split into four distinct peaks, corresponding to Fe − O (532.10 eV), C = O (531.28 eV), C − O (532.10 eV) and –OH (533.37 eV) [22,42,43].

The N 1 s XPS spectrum (Fig. 2e) of Fe@N − SBC was deconvolved into five characteristic peaks at 397.84 eV, 398.59 eV, 399.44 eV, 400.95 eV, 403.24 eV, corresponding to pyridinic N, pyrrole N, Fe − N_x, graphitic N and oxide N, respectively [25,39]. Studies have shown that pyridine N can form metal − N coordination structures with metal atoms due to the abundant coordination groups [44]. The high-resolution Fe 2p spectrum (Fig. 2f) was used to identify the valence states of Fe species in Fe@N − SBC. Peaks at 711.00 eV and 724.22 eV corresponded to Fe $2p_{3/2}$ and Fe $2p_{1/2}$, respectively, with satellite peaks at 719.59 eV and 732.95 eV, which were indexed to Fe(III) [45–47]. The binding energy peaks at 714.69 eV and 727.84 eV were attributed to Fe(II) $2p_{1/2}$ of Fe (II) and its satellite peak, indicating the existence of Fe^{2+} species in Fe@N − SBC [48]. The Fe 2p spectrum confirmed the co − existence of the Fe_2O_3 and Fe_3O_4 phases in the Fe@N − SBC catalyst. It was reported that Fe(II) and Fe(III) can coordinate with pyridine N to form Fe − N_x species in the catalyst [49]. Comparison with the XPS full-scan spectrum of SBC further indicates that external Fe and N doping is essential to enrich active sites and enhance PI activation (Text S6 and Table S7). Overall, the comprehensive characterization confirmed that the synthesized Fe@N − SBC had been inspected and was suitable for subsequent degradation experiments.

3.2. Adsorption and catalytic activity of Fe@N − SBC and coexisting matters effect

The adsorption performance of the material was first evaluated. The adsorption capacity at different BPA concentrations is measured to survey the adsorption property of Fe@N − SBC for BPA, as shown in Fig. 3a. The adsorption capacity increased with rising BPA concentration, reaching a maximum theoretical adsorption capacity of 61.0 mg g^{-1} determined for Fe@N − SBC, which is approximate to the actual value (46.5 mg g^{-1}). Fig. 3b illustrates the time-dependent adsorption behavior of BPA onto Fe@N − SBC. In the initial 30 min, the adsorption of BPA proceeded rapidly and eventually reached equilibrium due to the saturation of binding sites. In addition, fitting results from adsorption isotherms and kinetic models indicated that BPA adsorption on Fe@N − SBC followed a chemical monolayer process (Text S7 and Fig. S19-20). To determine the optimal dosage of $FeSO_4{\cdot}7H_2O$ and NH_4Cl, the BPA removal efficiency of catalysts prepared with different Fe/N mass ratios was evaluated (Fig. S2). In the Fe@N − $SBC_{2:1}$/PI system, Fe@N − $SBC_{1:1}$/PI system and the Fe@N − $SBC_{1:2}$/PI system, the BPA removal efficiencies were 96.1 %, 81.6 % and 86.0 %, with corresponding rate constants of 0.059 min^{-1}, 0.031 min^{-1} and 0.035 min^{-1}. Therefore, Fe@N − $SBC_{2:1}$ was identified as the optimal catalyst (hereafter referred to as Fe@N − SBC). The lower removal efficiencies of other Fe/N ratios could be ascribed to alterations in surface functional groups and the distribution of active sites. The pyrolysis temperature significantly influences the catalyst's structure, including functional groups, metal sites, and defect levels [49]. Therefore, the BPA removal efficiency of catalysts prepared at different calcination temperatures was evaluated (Fig. 3c). During the adsorption phase, the BPA adsorption capacity of

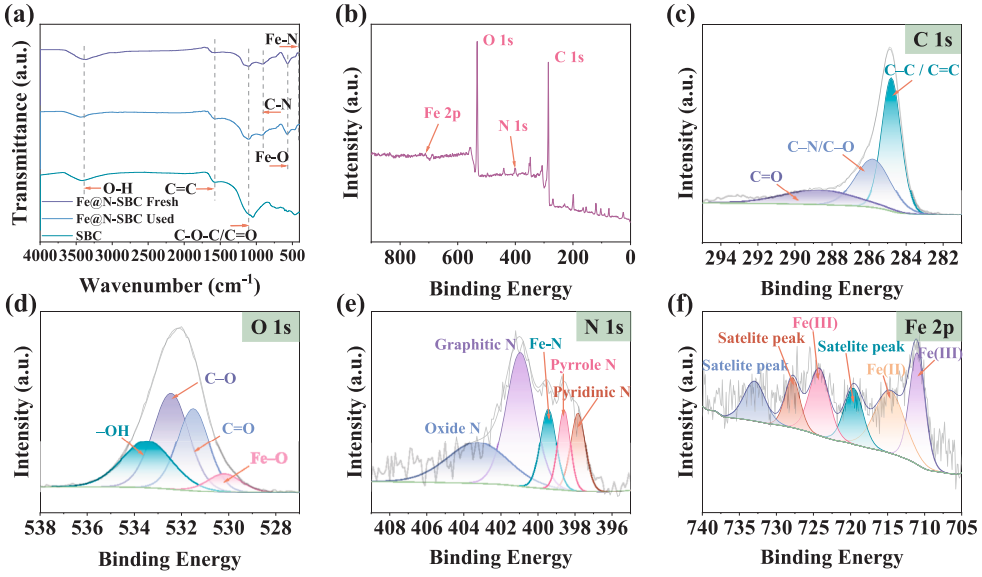

Fig. 2. (a) FTIR spectroscopies of SBC, fresh Fe@N − SBC and used Fe@N − SBC, (b) XPS full − scan spectrum of Fe@N − SBC includes (c) C 1 s, (d) O 1 s, (e) N 1 s and (f) Fe 2p.

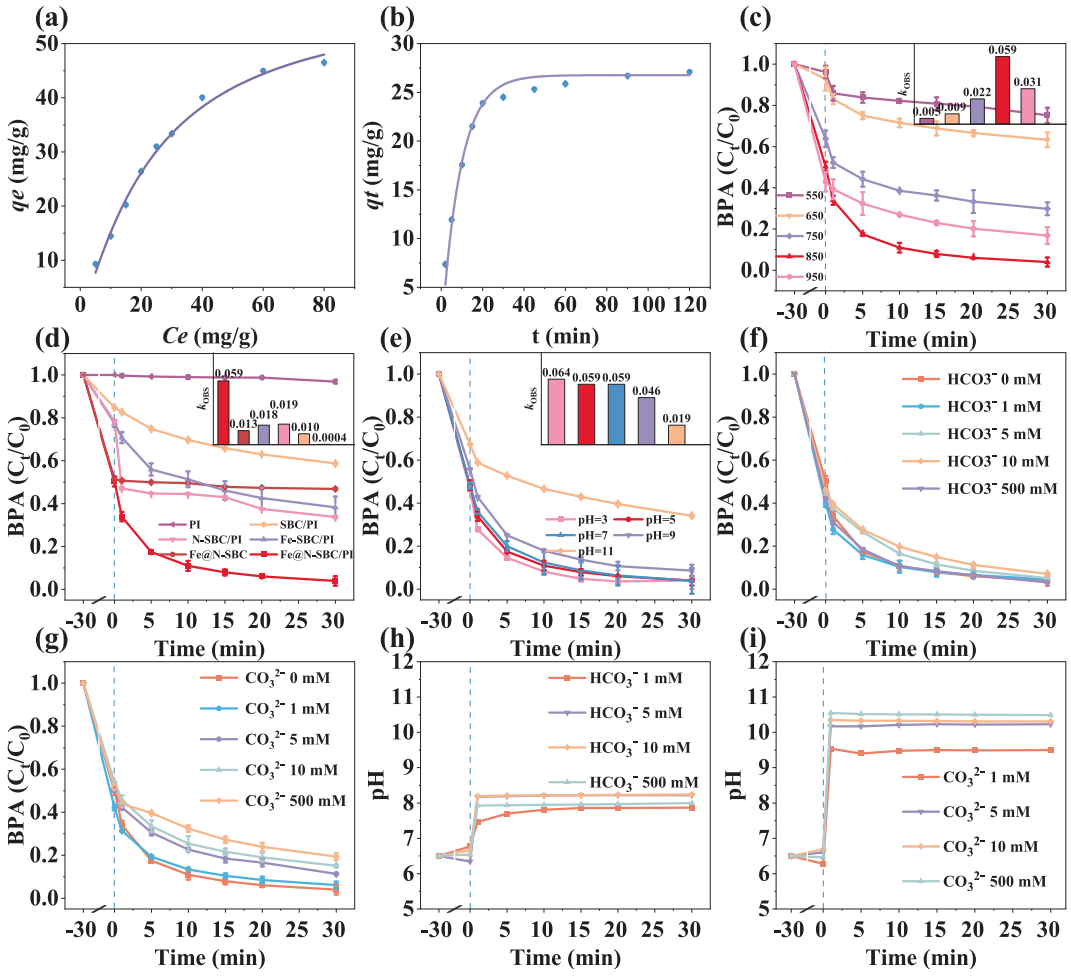

Fig. 3. (a) Adsorption isotherm and (b) time-dependent adsorption for BPA adsorption on Fe@N − SBC, effect on (c) different pyrolysis temperatures, (d) various systems and (e) initial pH on BPA removal (insert: pseudo-first order rate constants for BPA removal in different reaction conditions), effect of different concentrations of (f) HCO_3^- and (g) CO_3^{2-} on BPA removal in the Fe@N − SBC/PI system, the variation of pH during the reaction after the addition of different concentrations of (h) bicarbonate and (i) carbonate (reaction conditions: [catalyst] = 0.4 g L^{-1}, [BPA] = 20 mg L^{-1}, [PI] = 0.5 mM, T = 25℃, initial pH = 7.0).

Fe@N − SBC increased with rising pyrolysis temperature, likely attributed to the higher annealing temperature, enhanced the specific surface area and pore distribution of the carbon material while promoting the formation of dominant active sites for BPA adsorption [41]. After adding PI to trigger the degradation reaction, BPA degradation was improved as the annealing temperature increased from 550 °C to 850 °C. However, further increasing the temperature to 950 °C resulted in a decreased removal efficiency (85.1 %). This was because excessively high pyrolysis temperatures can disrupt active sites and reduce the degree of defects [50]. In addition, the *k* values of Fe@N − SBC at different annealing temperatures throughout the reaction stages are as follows: 550 °C (0.005 min^{-1}) < 650 °C (0.009 min^{-1}) < 750 °C (0.022 min^{-1}) < 950 °C (0.031 min^{-1}) < 850 °C (0.059 min^{-1}). Therefore, Fe@N − SBC pyrolyzed at 850 °C was selected as the optimal catalyst for further investigation.

To evaluate the performance of Fe@N − SBC in BPA removal, a series of control experiments were conducted, including PI alone, SBC/PI, N − SBC/PI, Fe − SBC/PI, Fe@N − SBC alone and Fe@N − SBC/PI. To distinguish the adsorption process from the catalytic degradation, a 30-minute pre − adsorption was conducted to achieve adsorption equilibrium. The control experiment using Fe@N − SBC alone demonstrated that adsorption equilibrium was reached within 30 min, and adsorption removal of BPA was 49.7 % (Fig. 3d). The degradation efficiency of BPA in the process using PI alone was only 3.1 % within 30 min, due to the low oxidation potential of IO_4^-. Surprisingly, the coupling of Fe@N − SBC with PI exhibited the highest removal efficiency (96.1 %) of BPA among all the tested biochar. The *k* value of Fe@N − SBC was approximately 3.3, 3.1 and 59.0 times greater than those of Fe − SBC, N − SBC and SBC, respectively. These results showed that Fe − modified and N − doped significantly enhance activation performance. During the catalytic process, the decomposition rates of PI by Fe@N − SBC, Fe − SBC, N − SBC, SBC and PI alone were 70.6 %, 19.0 %, 29.7 %, 12.8 % and 1.7 %, respectively, demonstrating the excellent catalytic performance of Fe@N − SBC. Moreover, no BPA was desorbed after the reaction, indicating that the BPA adsorbed on Fe@N − SBC was completely degraded (Fig. S3). In addition, optimization experiments were conducted for the Fe@N − SBC/PI system, including catalyst and PI dosages, BPA concentration, and reaction temperature (Text S7 and Fig. S21). The optimal reaction conditions were determined to be [Fe@N − SBC] = 0.4 g L^{-1}, [BPA] = 20 mg L^{-1}, [PI] = 0.5 mM and T = 25 °C. It is worth noting that although environmental BPA concentrations typically range from ng L^{-1} to μg L^{-1}, laboratory studies commonly use higher concentrations to clearly monitor degradation kinetics and catalyst performance. Additionally, this concentration is significant for evaluating potential treatment options in emergency leakage scenarios or in regions where strict BPA regulations are lacking.

It was well known that initial pH is an essential factor influencing both pollutant degradation rate and catalyst performance. Hence, control experiments were conducted over a pH range of 3.0 to 11.0 to evaluate changes in removal efficiency and catalyst performance in the

Fe@N − SBC/PI systems. Fig. 3e suggests that the removal rate of BPA remained above 90 % across pH values from 3.0 to 9.0. Moreover, a similar k was observed at pH = 3 (0.064 min^{-1}), 5 (0.059 min^{-1}) and 7 (0.059 min^{-1}) and 9 (0.046 min^{-1}). It is worth noting that the removal rate of BPA significantly decreased to 65.9 % at pH 11.0, much lower than those observed at pH values between 3.0 and 9.0. This decline can be attributed to two main factors. First, the high reduction potential of IO_4^-/IO_3^- (IO_4^-/IO_3^- = 1.298 V) will convert to its dimerized form, $H_3IO_6^{2-}$, which has a lower reduction potential ($H_3IO_6^{2-}/IO_3^-$ = 0.686 V) [38]. Second, BPA may deprotonate in a basic environment, which causes electrostatic repulsion between the contaminant and Fe@N − SBC (discussed in Section 3.4).

Studies have shown that the addition of CO_3^{2-}/HCO_3^- can rapidly increase solution pH, making it more alkaline [51]. As shown in Fig. 3f-g, the BPA removal rate decreased from 98.1 % to 80.6 % as the concentration of CO_3^{2-} in the solution increased from 1 mM to 500 mM; and when the HCO_3^- concentration was increased from 1 mM to 500 mM, the BPA removal rate decreased to 92.9 %. To verify their influence on pH, the changes in pH of BPA solutions with different concentrations of CO_3^{2-} and HCO_3^- were measured (Fig. 3 h-i). Obviously, after the addition of CO_3^{2-} and HCO_3^-, the solution pH rapidly shifted to alkaline. In addition, CO_3^{2-} and HCO_3^-may inhibit the formation of $^1O_2$, thereby reducing the pollutant removal efficiency [52]. Furthermore, a series of condition optimizations were conducted, including catalyst and PI dosages, BPA concentration and temperature (Text S8). 0.4 g L^{-1} Fe@N − SBC with 0.5 mM PI at 25℃ was selected as the optimal condition. Other common coexisting anions (SO_4^{2-}, $H_2PO_4^-$, Cl^- and HA) exhibited only minor inhibitory effects on BPA removal (Text S9 and Fig. S22).

3.3. Mechanistic insights into BPA degradation and possible PI activation pathway

Previous studies suggested that multiple reactive species, including ROS (hydroxyl radicals ($^{\bullet}OH$), superoxide radicals ($O_2^{\bullet-}$), singlet oxygen ($^1O_2$) and RIS ($IO_3^{\bullet}$ and $IO_4^{\bullet}$), contribute to pollutant degradation in PI oxidation systems. Quenching experiments were conducted to elucidate their roles in BPA degradation and potential PI activation pathways [53]. MeOH and TBA (k = (3.8–7.6) × 10^8 mol $L^{-1}s^{-1}$) can be an $^{\bullet}OH$ quencher [54]. The results showed that the inhibitory effects of 500 mM MeOH and TBA on BPA degradation were minimal, suggesting that $^{\bullet}OH$ is not the primary reactive species (Fig. 4, S4 and S5 a-b). FFA was applied as a quenching agent for $^1O_2$ with k = 1.2 × 10^8 $M^{-1}s^{-1}$ [55]. Surprisingly, FFA significantly inhibits the degradation of BPA from 100 % to 69.2 % (Fig. 4b), reducing k to 0.021 min^{-1} (with 20 mM FFA), which was lower than 0.059 min^{-1} (without scavenger), suggesting that $^1O_2$ may be one of the main oxidizing species (Fig. S5d). Nevertheless, it is important to note that FFA tends to consume PI through direct electron transfer [56]. To investigate the reason for the inhibited BPA degradation efficiency after the addition of the FFA scavenger, the PI − only system was implemented to verify whether the decrease in degradation rate was caused by the direct consumption of PI by FFA (Fig. S6). The results showed that PI was not degraded in the presence of FFA at different concentrations, supporting the generation of $^1O_2$ in the Fe@N − SBC/PI system. Phenol has been reported to quench $IO_3^{\bullet}$ [57]. Its presence can be indirectly confirmed through scavenging experiments. About 31 % of BPA removal was suppressed with the addition of phenol, indicating the contribution of $IO_3^{\bullet}$ to BPA removal (Fig. 4c). According to previous studies, 2,4,6 − TCP cannot be removed by $IO_3^{\bullet}$ [58]. Using 2,4,6 − TCP as the target contaminant, the degradation efficiency in the Fe@N − SBC/PI system was 99.6 %, further confirming the presence of other active species in the system ($^{\bullet}OH$ and $^1O_2$) (Fig. S7). In addition, quenching experiments with p-BQ and DMSO excluded the contributions of $O_2^{\bullet-}$ and high-valent Fe species, respectively (Text S10 and Fig. S23). Furthermore, the contribution of active species to BPA degradation in Fe@N − SBC/PI system was quantified (Table S8-9). The calculation showed that the contribution of $^{\bullet}OH$, $IO_3^{\bullet}$ and $IO_3^{\bullet}$ to the degradation of BPA were 14.4 %, 50.3 %, and 35.3 %.

EPR spectroscopy was performed using DMPO and TEMP as trapping agents to verify the generation of reactive oxidizing species. As expected, no obvious characteristic peaks were observed in DMPO/PI, DMPO/Fe@N − SBC, TEMP/PI, or TEMP/Fe@N − SBC, proving that neither PI nor SBC alone could generate ROS. Unlike previous studies, no characteristic signals of DMPO−$^{\bullet}OH$ adduct (with the hyperfine splitting of 1:2:2:1) were detected, implying an apparent absence of $^{\bullet}OH$. However, quenching experiments had confirmed the contribution of $^{\bullet}OH$ in the BPA degradation process, which contradicts the results of the EPR experiments. A characteristic signal with hyperfine splitting of 1:2:1:2:1:2:1 was observed when DMPO was used as the trapping agent,

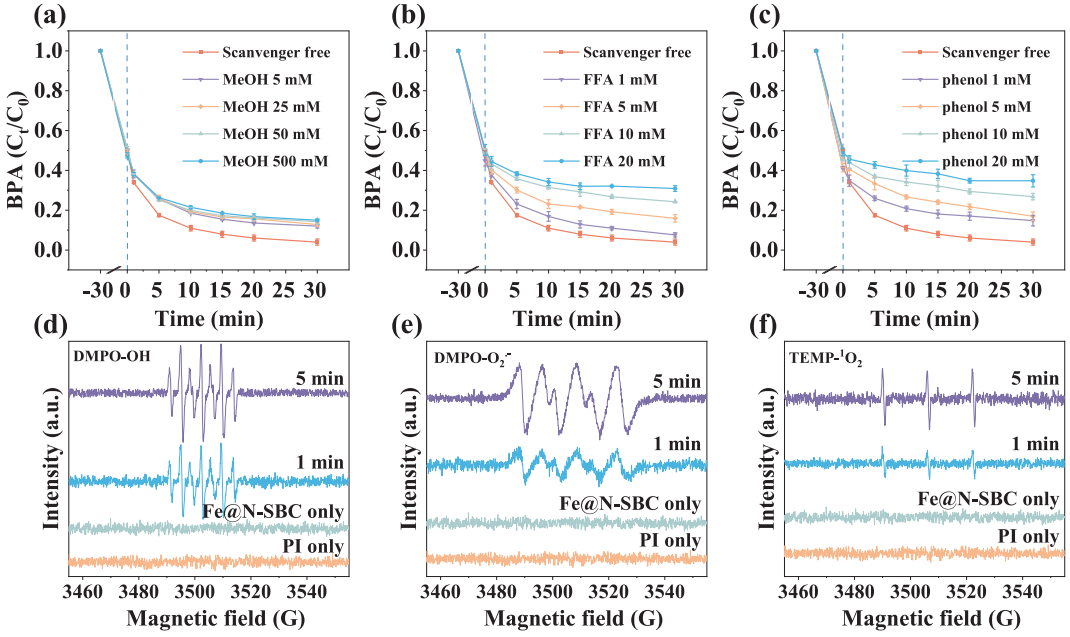

Fig. 4. Effect of different concentrations of quenchers on BPA degradation in the Fe@N − SBC/PI system: (a) MeOH, (b) FFA and (c) phenol, EPR spectra of (d) DMPO−$^{\bullet}OH$, (e) DMPO − $O_2^{\bullet-}$ and (f) TEMP−$^1O_2$ (reaction conditions: [catalyst] = 0.4 g L^{-1}, [BPA] = 20 mg L^{-1}, [PI] = 0.5 mM, T = 25℃, initial pH = 7.0).

which corresponds to the signature signal of 5,5 − dimethyl − 1 − pyrrolidone − 2 − oxyl (DMPOX) (Fig. 4d) [59].

Previous studies showed that DMPOX adducts can be generated through direct reaction with $^1O_2$ and a mediated electron transfer process [60]. To evaluate the role of electron transfer in DMPOX formation, electrochemical experiments were conducted (Text S11 and Fig. S24b). The results revealed minimal current change after the addition of PI to the Fe@N − SBC/PI system, confirming that $^1O_2$ directly reacted to form the DMPOX adduct. To further verify $^{\bullet}OH$ generation, the EPR spectra of the DMPO/Fe@N − SBC/PI system were monitored in the presence of 20 mM FFA. A strong signal with hyperfine splitting of 1:2:2:1 appeared, corresponding to the DMPO−$^{\bullet}OH$ adduct (Fig. S8). As shown in Fig. 4e, the EPR spectra related to DMPO − $O_2^{\bullet-}$ (with the hyperfine splitting of 1:1:1:1) are detected [61]. Considering its lower redox potential (E^0 ($O_2^{\bullet-}/O_2$) = − 0.33 V) and the results from quenching experiments, $O_2^{\bullet-}$ is likely an intermediate that transforms into other reactive species [62]. Moreover, the particular spectrum (with the hyperfine splitting of 1:1:1) can be observed, which was the characteristic signal of the TEMP-$^1O_2$ adduct (Fig. 4f) [63]. The discussion of the quenching and EPR experimental results suggested that $^1O_2$ and $IO_3^{\bullet}$ played a leading role in BPA removal, followed by $^{\bullet}OH$.

3.4. Evolution mechanism

All the above data indicated that the Fe@N − SBC/PI system removed BPA through both adsorption and catalytic processes. Regarding adsorption, Text S12 elucidated that electrostatic interaction, π–π electron donor–acceptor (EDA) interaction, hydrogen bonding and surface complexation synergistically governed the adsorption process. Specifically, electrostatic repulsion under alkaline conditions, enhanced π–π EDA interaction due to graphitization, increased − OH content promoting hydrogen bonding and Fe–O coordination indicating surface complexation collectively contributed to adsorption of BPA (Fig. 5a–e and S25-S26). Adsorption isotherms and kinetic fitting indicate that surface complexation and π–π EDA interactions are the predominant adsorption mechanisms (Text S7).

In terms of catalytic removal, XPS spectra of used Fe@N − SBC were analyzed to investigate active sites and underlying catalytic mechanisms. Studies have shown that the transformation of C=C bonds into C − O/C − N bonds was considered to activate PI [64]. The proportion of C=C bonds decreased from 59.3 % to 55.9 %, while the proportion of C − O/C − N bonds increased from 40.7 % to 44.1 % after the reaction, indicating that a catalytic reaction involving C=C bond cleavage and C − O/C − N bond formation occurred. Moreover, the ratio of C=O decreased from 24.3 % to 15.8 %, suggesting that C=O acts as an electrophilic site to facilitate $^1O_2$ generation. Regarding N configuration, the ratio of pyridinic N dropped from 13.4 % to 8.8 %, implying that the pyridinic N served as one of the active sites of Fe@N − SBC (Fig. 5f). Pyridinic N can promote oxidant adsorption by inducing positive charge on adjacent carbon atoms and donating electrons to PI for its activation, and a higher pyridinic N content provides more catalytic sites by increasing the density of structural defects [31]. Additionally, the percentage of Fe − N_x bonds was reduced from 14.5 % to 5.1 %, confirming that Fe − N_x sites serve as the main active site in PI activation. The Fe − N_x structure stabilizes the coordination environment of Fe in Fe@N − SBC and enhances the availability of Lewis acid sites, thereby facilitating PI adsorption and polarization [65]. Previous studies have proposed that Fe (II) can activate PI and be oxidized to Fe (III) [66]. From the Fe 2p spectra, the Fe (II)/Fe (III) ratio in Fe@N − SBC shifted from 38.1 %/61.9 % before the reaction to 26.4 %/73.6 % after the degradation process. This change indicates that Fe(II) acted as an electron donor to PI and produced $^{\bullet}OH$ and $O_2^{\bullet-}$ during catalytic decomposition, consistent

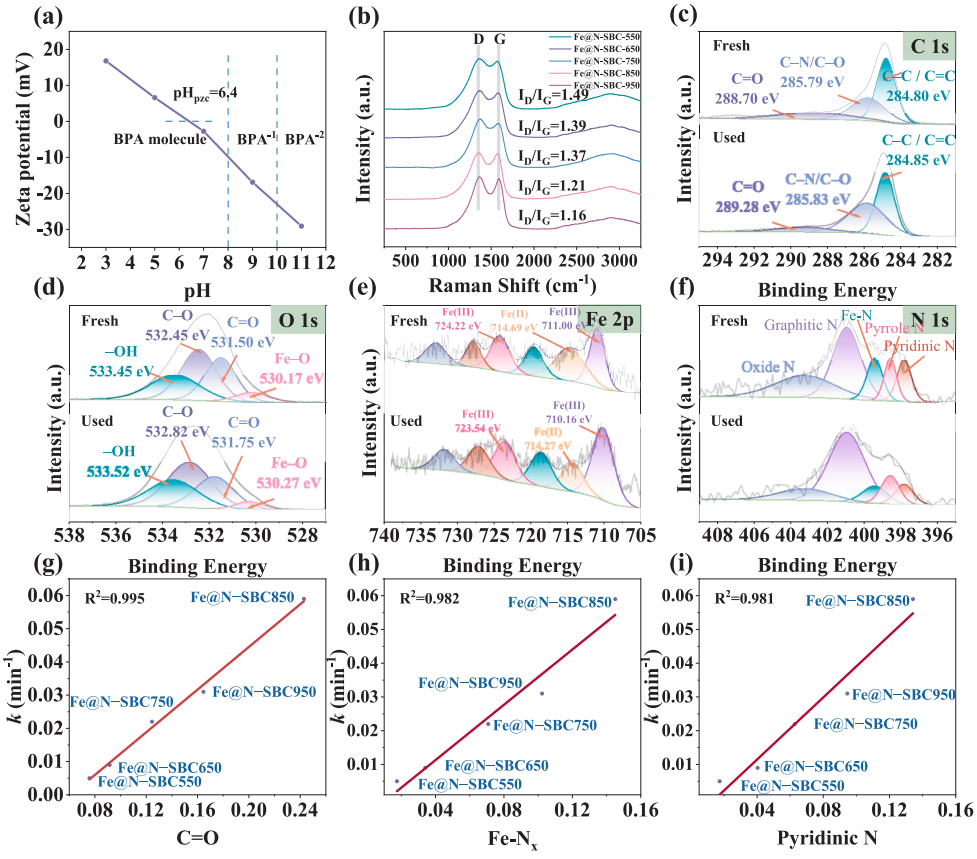

Fig. 5. (a) Zeta potential of Fe@N − SBC across a pH range of 3–11, (b) Raman spectra of Fe@N − SBC − x, high − resolution spectra of (c) C 1 s, (d) O 1 s, (e) Fe 2p and (f) N 1 s of fresh and used Fe@N − SBC, relationship of reaction rate to (g) C = O, (h) Fe − N_x and (i) pyridinic N.

with the established mechanism of heterogeneous activation by iron-based catalysts [31,67].

To further elucidate the contribution of active sites, the relationship between functional groups in Fe@N − SBC synthesized at different temperatures and their *k* was investigated. A positive correlation was observed between the reaction rate and the proportions of C=O (R^2 = 0.995), Fe − N_x (R^2 = 0.982), and pyridinic N (R^2 = 0.981), confirming their crucial role as active sites in PI activation (Fig. 5 g-i). The Fe (II)/Fe (III) ratio showed a strong correlation with the k value (R^2 = 0.978), further confirming the Fe (II) − induced radical pathway (Fig. S9a). Additionally, C − C/C=C and C − O/C − N bonds, graphite N, pyrrolic N and oxide N showed no significant correlation with *k* (Fig. S9b-f).

To gain a deeper understanding of the adsorption and catalytic mechanisms at the molecular and atomic levels, density functional theory (DFT) calculations are conducted. The optimized structures of Fe@N − SBC and SBC are shown in Fig. S10. As shown in Fig. 6a-b, the corresponding BPA adsorption energies on SBC and Fe@N − SBC are −0.86 and −2.03 eV, indicating that Fe and N doping enhanced the adsorption capacity of materials.

To further explore the molecular interactions, electron distribution, and bonding characteristics involved in the adsorption process, the Independent Gradient Model based on Hirshfeld partition (IGMH), electrostatic potential (ESP), and electron localization function (ELF) was conducted [68,69]. Comparing IGMH of SBC (Fig. 6e) and Fe@N − SBC (Fig. 6f), it is observed that the δ_g peak associated with hydrogen bonding in Fe@N − SBC is significantly higher than that in SBC, suggesting that Fe@N − SBC is more prone to forming hydrogen bonds with BPA. ESP analysis revealed that Fe@N − SBC exhibited more pronounced electrostatic potential fluctuations compared to SBC, indicating a greater heterogeneity in surface charge distribution (Fig. 6c-d). This suggests that Fe@N − SBC can engage in diverse adsorption interactions, such as electrostatic interactions and π–π stacking. Fig. 6 g-h shows that the high ELF value (ELF > 0.8) is near the Fe–O coordination region and primarily localized on the oxygen atom of BPA, which indicates the bonding nature of the Fe − O interaction. Specifically, the lone pair electrons on the hydroxyl oxygen of BPA remain strongly localized while participating in orbital overlap with the empty d-orbitals of the Fe center, leading to the formation of a stable chemisorption structure.

Similarly, optimized adsorption models of PI on SBC and Fe@N − SBC were constructed to reveal the interactions between PI and the active sites. As demonstrated in Fig. 6i-j, the adsorption energy of PI on Fe@N − SBC (−4.86 eV) is higher than that on SBC (−1.30 eV), suggesting a strong adsorption affinity between Fe@N − SBC and PI. Meanwhile, the I − O bond length of PI adsorbed on Fe − N sites (2.31Å) or surface Fe oxides (2.28 Å) in Fe@N − SBC was longer than that on SBC (2.17Å), which made the I − O bond easier to cleave. Furthermore, Bader charge analysis revealed that Fe@N − SBC (1.12 e) was more capable of transferring electrons to IO_4^- compared to SBC (0.83 e) (Fig. 6 k-l). Charge density difference results showed that Fe and N doping adjusted the spin density and charge distribution, thereby enhancing the reactivity of the inert carbon framework. Moreover, the total density of states (TDOS) and partial density of states (PDOS) of different elements were calculated to intuitively reveal the electronic structure characteristics of the material [70]. Fe@N − SBC exhibited a higher density of states near the Fermi level compared to SBC, which is favorable for enhancing electronic polarization interactions with PI molecules (Fig. 6m) [71]. In addition, Fe@N − SBC exhibited a distinct non-zero density of states at the Fermi level (0 eV), indicating metallic or semi-metallic characteristics, which favors electron transfer and facilitates

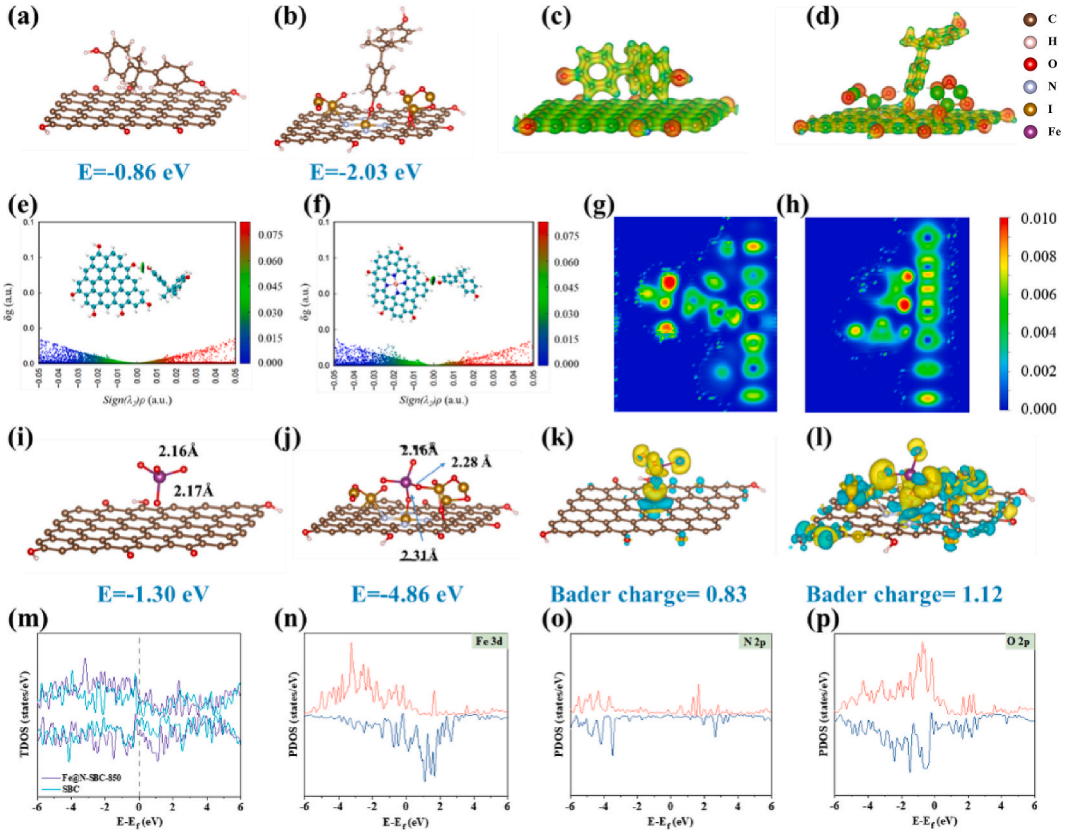

Fig. 6. Optimized adsorption model for BPA on the surface of (a) SBC, (b) Fe@N − SBC and (c-d) ESP maps, IGMH analysis for BPA on the surface of (e) SBC and (f) Fe@N − SBC, ELF analysis for BPA on the surface of (g) SBC and (h) Fe@N − SBC; Optimized adsorption model for IO_4^- on the surface of (i) SBC and (j) Fe@N − SBC, sideview of charge density difference distribution of IO_4^- on (k) SBC and (l) Fe@N − SBC, (m) TDOS diagram for SBC and Fe@N − SBC and PDOS diagram for (n) Fe 3d, (o) N 2p and (p) O 2p of Fe@N − SBC model.

the generation of reactive radicals. As shown in Fig. 6n, the presence of pronounced Fe 3d orbital peaks near the Fermi level suggests a half-filled electronic state with strong orbital coupling potential with O or I atoms [72]. Fig. 6o shows that the PDOS of N exhibited dense peaks below the Fermi level, attributed to the lone pair electrons of pyridinic N, indicating its potential as an electron donor in the coordination adsorption of IO_4^-. The PDOS of O atoms exhibited a broad energy distribution, which was due to the coexistence of Fe–O and C=O, indicating their important role in electronic regulation and the formation of active sites (Fig. 6p). DFT analysis further confirmed that BPA adsorption onto Fe@N–SBC brings BPA molecules into proximity to catalytic active sites such as Fe–N_x and pyridinic N. Compared to free BPA in aqueous solution, the adsorption process shortens the reaction pathway between BPA and the reactive species, thus promoting the removal rate of BPA.

Overall, Fe–N_x is identified as the primary active site for PI activation by Fe@N–SBC, as it provides a stable coordination environment and elongates the I − O bond of PI, thereby facilitating bond cleavage. The variation in Fe(II) and Fe(III) contents before and after the reaction indicates that the Fe(II)/Fe(III) redox cycle acts as a secondary contributor to PI activation. Although pyridinic N and C=O groups are not the dominant functional groups in the Fe@N–SBC/PI system, their auxiliary roles in promoting ROS generation and BPA adsorption should not be overlooked.

3.5. Degradation pathways of BPA and toxicity assessment

DFT calculations were conducted on BPA to identify molecular sites susceptible to oxidative attack. The highest occupied molecular orbital (HOMO) and lowest unoccupied molecular orbital (LUMO) were analyzed to depict potential electron-donating and electron-accepting regions/sites during the oxidation process [73]. As shown in Fig. 7a − c, C3, C6, C13, C16 and C23 are prone to electron loss and susceptible to undergoing oxidation reactions, whereas C1, C2, C4, C5, C17 − C19 and C21 are easy to gain electrons and undergo reduction reactions. Additionally, the molecular ESP was calculated to visualize the surface electron density distribution of BPA (Fig. 7d) [74]. The phenolic hydroxyl groups and adjacent carbon atoms exhibit negative electrostatic potential, suggesting that electrophilic reactions are more likely to occur at these sites. To further identify the vulnerable sites of BPA, the condensed Fukui function was calculated, where f^-, f^+ and f^0 correspond to the site reactivity toward electrophilic, nucleophilic and radical attacks, respectively [75]. Fig. 7e − f and Fig. 7h indicate that O32, O12, C23, C19, C3, C2, C16 and C6 are the primary electrophilic sites owing to their higher f^- values, while the relatively high f^0 values of C19, C2, O32, C4, O12, C21, C1 and C17 suggest that these atoms are the main active sites for radical attacks. The absolute values of the condensed dual descriptor (CDD) can reflect the propensity strength of each site to be attacked (Fig. 7g) [76]. The results indicate that the phenolic hydroxyl group and the benzene ring exhibit a notable tendency to be attacked.

The possible degradation pathways of BPA were further investigated by LC-MS analysis (Fig. 7i and S10). Initially, the radical attack by $^{\bullet}OH$ and $IO_3^{\bullet}$ led to the oxidation of the aromatic ring in BPA, forming P1 ($m/z = 293$) [77]. Additionally, hydroxylation occurred at the carbon atoms adjacent to the hydroxyl groups of BPA, producing the addition product P2 ($m/z = 259$) [78]. Subsequently, P1 and P2 underwent oxidation to form quinone intermediate P3 ($m/z = 255$). Further oxidation and ring cleavage reactions resulted in the formation of P4 ($m/z = 275$) and P5 ($m/z = 175$). Moreover, BPA also underwent β-cleavage and demethylation in the presence of $^1O_2$, forming phenolic free radicals [79], which further underwent coupling and hydroxylation reactions to produce P6 ($m/z = 219$) and P7 ($m/z = 231$) [80]. Additionally, BPA could also undergo direct hydroxylation and ring cleavage to generate P8 ($m/z = 339$) [78]. Finally, P4, P5, P7, and P8 were decomposed into P9 ($m/z = 61$), P10 ($m/z = 113$), P11 ($m/z = 117$) and P12 ($m/z = 85$) through ring cleavage reactions, and then converted to H_2O and CO_2 through mineralization. Toxicity assessments confirmed that the Fe@N − SBC/PI system reduced the biotoxicity of BPA (Text S13 and Fig. S27). Moreover, no toxic iodine species (e.g., HOI, I_2, I_3^-) or iodinated by-products were detected, demonstrating the environmental safety of the system (Text S14 and Fig. S28).

3.6. Stability of the catalysts

The stability and reusability of Fe@N − SBC were evaluated through four consecutive cycles of BPA degradation under identical conditions. As shown in Fig. S12, the BPA removal efficiency slightly decreases with increasing cycles. In the fourth cycle experiment, the BPA degradation rate dropped to 66.2 %. The deterioration in recycling performance may be attributed to the depletion of active sites during PI activation and the adsorption of intermediates on the catalyst, which hinder its ability to adsorb both the oxidant and the pollutant [81,82]. Re-calcination of Fe@N − SBC may regenerate active sites and remove adsorbed organic pollutants and their degradation intermediates from the catalyst. Furthermore, no significant changes were observed in the XRD patterns of fresh and used Fe@N − SBC, indicating the structural and crystalline stability of Fe@N − SBC (Fig. S13). Meanwhile, the leaching of Fe ions remained below 6 μg L^{-1} at a dosage of 0.4 g L^{-1} Fe@N − SBC in Fig. S14, which is significantly lower than the limit specified in the Chinese Standards for Drinking Water Quality (GB5749-2006) [67]. Thus, the leaching of Fe was allowed according to the standards and had negligible effect on BPA degradation. It is worth noting that the Fe@N − SBC/PI system exhibits a significant advantage in the degradation of organic pollutants compared to previously reported reaction systems (Fig. S15 and Table S10). As shown in Fig. S16, the Fe@N − SBC/PI system achieves a total organic carbon (TOC) removal efficiency of 73.9 % by the end of the reaction. High TOC removal efficiency is not only due to the mineralization of BPA but also attributed to the oxidation of BPA by reactive species, which is then degraded into intermediate products and adsorbed onto Fe@N − SBC. Additionally, Fe@N − SBC/PI system exhibited broad-spectrum efficacy in removing contaminants such as sulfamethoxazole (SDZ), pharmaceuticals and personal care products (ACE) and quinolones (CIP) (Fig. S17). In conclusion, Fe@N − SBC exhibited stable morphology and structure, demonstrating excellent catalytic stability in PI activation.

4. Conclusion

In this study, a novel Fe and N co-doped biochar (Fe@N − SBC) was successfully synthesized via a facile pyrolysis method using sewage sludge as the precursor. The resulting material exhibited excellent adsorption capacity and catalytic activity for BPA removal in a PI-based advanced oxidation process. Comprehensive investigations revealed that the removal process involved both adsorption and catalysis. The primary adsorption mechanisms included π–π EDA interactions, electrostatic interactions, hydrogen bonding and surface complexation. Catalytic degradation of BPA was primarily driven by the synergistic action of radical ($^{\bullet}OH$ and $IO_3^{\bullet}$) and non-radical ($^1O_2$) pathways. Active species were verified through quenching experiments and EPR spectroscopy, while XPS analysis revealed that Fe–N_x, pyridinic N, C=O and Fe(II)/Fe(III) redox cycling were the key active sites for PI activation. Additionally, DFT supported the proposed adsorption and catalytic reaction pathways and elucidated the electronic structure and reactive sites of the catalyst. Importantly, no toxic iodine species or iodinated by-products were formed during the reaction, indicating the environmental safety of the system. This work provides new insights into the design of low-cost, sludge-derived multifunctional catalysts for efficient and safe wastewater remediation.

Declaration of competing interest

The authors declare that they have no known competing financial interests or personal relationships that could have appeared to influence

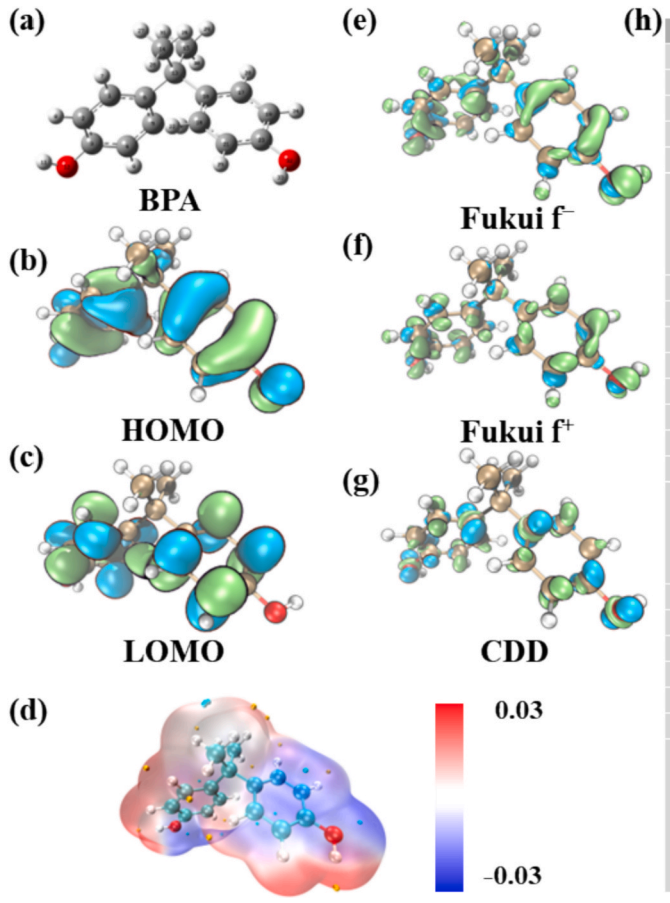

(h)

Atom	f^-	f^+	f^0	CDD
1(C)	0.0334	0.0608	0.0471	0.0274
2(C)	0.0509	0.0628	0.0568	0.0119
3(C)	0.0536	0.0302	0.0419	-0.0234
4(C)	0.0357	0.0657	0.0507	0.0301
5(C)	0.0274	0.0468	0.0371	0.0194
6(C)	0.0474	0.0122	0.0298	-0.0351
7(H)	0.0218	0.0304	0.0261	0.0087
8(H)	0.0292	0.0354	0.0323	0.0063
9(H)	0.0255	0.0352	0.0303	0.0097
10(H)	0.0159	0.0234	0.0196	0.0075
11(H)	0.0279	0.0193	0.0236	-0.0086
12(O)	0.0713	0.0286	0.0499	-0.0427
13(C)	0.0037	-0.0007	0.0015	-0.0044
14(C)	0.0115	0.0092	0.0104	-0.0023
15(C)	0.0114	0.0092	0.0103	-0.0022
16(C)	0.0485	0.0121	0.0303	-0.0364
17(C)	0.0309	0.0599	0.0454	0.029
18(C)	0.0318	0.0469	0.0394	0.0151
19(C)	0.0543	0.0645	0.0594	0.0102
20(H)	0.0215	0.03	0.0258	0.0085
21(C)	0.0347	0.0635	0.0491	0.0289
22(H)	0.017	0.0235	0.0203	0.0065
23(C)	0.0547	0.0304	0.0425	-0.0243
24(H)	0.0302	0.0361	0.0331	0.0058
25(H)	0.0252	0.0343	0.0298	0.0091
26(H)	0.0158	0.0153	0.0156	-0.0004
27(H)	0.0175	0.0155	0.0165	-0.0021
28(H)	0.0087	0.0103	0.0095	0.0017
29(H)	0.0173	0.0155	0.0164	-0.0017
30(H)	0.0088	0.0103	0.0096	0.0015
31(H)	0.0157	0.0153	0.0155	-0.0005
32(O)	0.0726	0.0292	0.0509	-0.0433
33(H)	0.0284	0.0186	0.0235	-0.0098

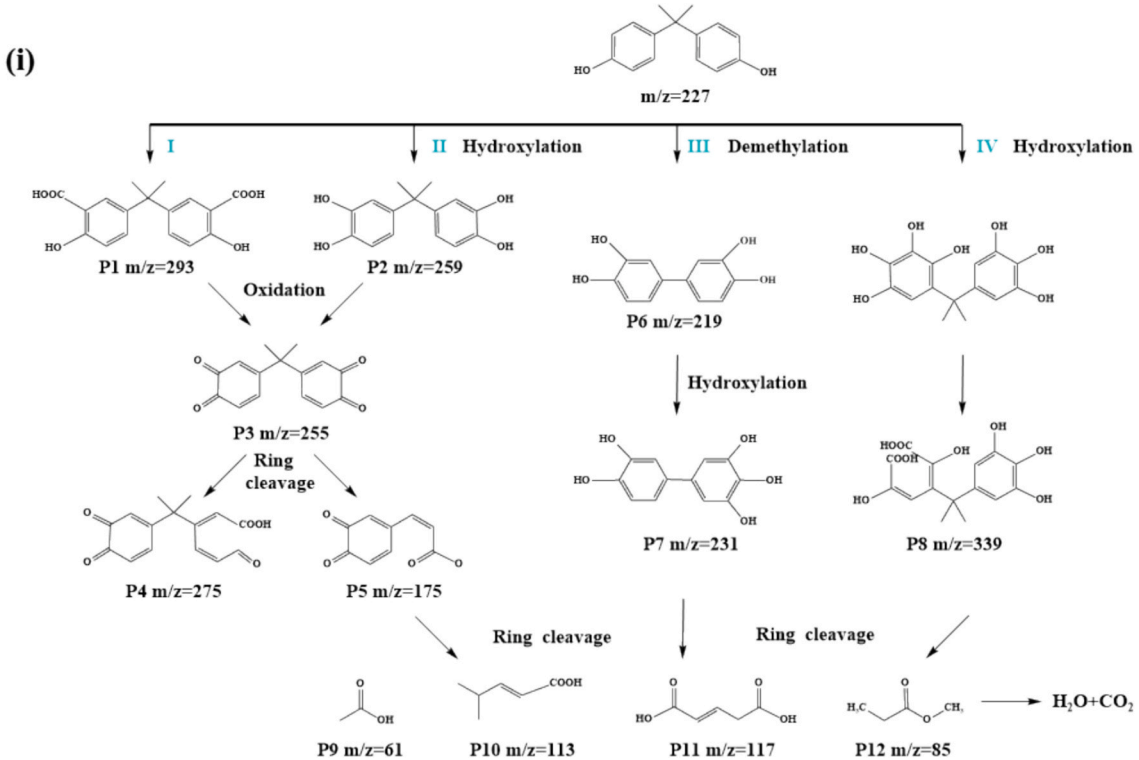

Fig. 7. (a) Optimized structure, (b) HOMO, (c) LOMO, (d) ESP and (e-g) condensed Fukui function isosurface maps of BPA, (h) fukui index f^-, f^+ and f^0 of BPA and (i) degradation pathways.

the work reported in this paper.

Acknowledgements

This work was supported by Tianjin Science and Technology Planning Project (Grant No. 24PTLYHZ00310).

Appendix A. Supplementary data

Supplementary data to this article can be found online at https://doi.org/10.1016/j.seppur.2025.135124.

Data availability

The data that has been used is confidential.

References

[1] K.L. Howdeshell, A.K. Hotchkiss, K.A. Thayer, J.G. Vandenbergh, F.S. Vom Saal, Exposure to bisphenol a advances puberty, Nature 401 (1999) 763–764, https://doi.org/10.1038/44517.
[2] W. Sun, Y. Lei, Z. Jiang, K. Wang, H. Liu, T., Xu, BPA and low-Se exacerbate apoptosis and mitophagy in chicken pancreatic cells by regulating the PTEN/PI3K/AKT/mTOR pathway, J. Adv. Res. (2024) S2090123224000420, https://doi.org/10.1016/j.jare.2024.01.029.
[3] L. Zhu, Y. Liu, X. Xue, C. Yuan, Z. Wang, BPA's transgenerational disturbance to transcription of ovarian steroidogenic genes in rare minnow Gobiocypris rarus via DNA and histone methylation, Sci. Total Environ. 762 (2021) 143055, https://doi.org/10.1016/j.scitotenv.2020.143055.
[4] M. Yuan, S. Chen, C. Zeng, Y. Fan, W. Ge, W. Chen, Estrogenic and non-estrogenic effects of bisphenol a and its action mechanism in the zebrafish model: an overview of the past two decades of work, Environ. Int. 176 (2023) 107976, https://doi.org/10.1016/j.envint.2023.107976.
[5] F.M. Mpatani, Adsorption performance of modified agricultural waste materials for removal of emerging micro-contaminant bisphenol a: a comprehensive review, Sci. Total Environ. 780 (2021) 146629, https://doi.org/10.1016/j.scitotenv.2021.146629.
[6] W. Tian, J. Han, L. Wan, N. Li, D. Chen, Q. Xu, H. Li, J. Lu, Enhanced piezocatalytic activity in ion-doped SnS_2 via lattice distortion engineering for BPA degradation and hydrogen production, Nano Energy 107 (2023) 108165, https://doi.org/10.1016/j.nanoen.2023.108165.
[7] K. Xu, Y. Li, Q. Li, G. Yi, R. Gao, K.H.D. Tang, E.F. Ali, S. Peter, S.M. Hooda, R. L. Shaheen, Biodegradation of bisphenol-a in water using a novel strain of Xenophilus sp. embedded onto biochar: Elucidating the influencing factors and degradation pathway, Journal of Hazardous Materials 477 (2024) 135239, https://doi.org/10.1016/j.jhazmat.2024.135239.
[8] Q. Wang, Y. Cao, M. Yu, G. Lv, C. Zhang, W. Wang, J. Jia, Z. Wang, Facile construction of Z-scheme AgBr/BiO$(HCOO)_{0.75}I_{0.25}$ photocatalyst for visible-light-driven BPA degradation: Catalytic kinetics, selectivity and mechanism, Separation and Purification Technology 302 (2022) 122087, https://doi.org/10.1016/j.seppur.2022.122087.
[9] E. Brillas, Degradation/mineralization of bisphenol a from aqueous matrices by single and combined electrochemical advanced oxidation processes, A Review, Separation and Purification Technology 357 (2025) 130170, https://doi.org/10.1016/j.seppur.2024.130170.
[10] Y. Liu, C. Yu, H. Lu, L. Liu, J. Tang, Silver and g-C3N4 co-modified biochar (Ag-CN@BC) for enhancing photocatalytic/PDS degradation of BPA: Role of carrier and photoelectric mechanism, Environ. Res. 262 (2024) 119972, https://doi.org/10.1016/j.envres.2024.119972.
[11] X. Wang, P. Zhang, S. Meng, C. Zhou, Z. Xiong, C. He, Y. Liu, H. Zhang, P. Zhou, B. Lai, Metal-free carbon nanotube boosted periodate oxidation towards organic pollutants: Identification of active sites and activation mechanism, Sep. Purif. Technol. 354 (2025) 129186, https://doi.org/10.1016/j.seppur.2024.129186.
[12] Y. Shen, J. Huang, J. Qiao, J. Chen, E. Batjargal, B.-A. Tuulaikhuu, Y. Qian, X. Zhou, Y. Zhang, Metal-based activation of periodate as an advanced oxidation process for water decontamination: a critical review, Chem. Eng. J. 513 (2025) 162949, https://doi.org/10.1016/j.cej.2025.162949.
[13] E.-T. Yun, H.-Y. Yoo, W. Kim, H.-E. Kim, G. Kang, H. Lee, S. Lee, T. Park, C. Lee, J.-H. Kim, J. Lee, Visible-light-induced activation of periodate that mimics dye-sensitization of TiO_2: Simultaneous decolorization of dyes and production of oxidizing radicals, Appl Catal B 203 (2017) 475–484, https://doi.org/10.1016/j.apcatb.2016.10.029.
[14] N.N. Mahamuni, Y.G. Adewuyi, Advanced oxidation processes (AOPs) involving ultrasound for waste water treatment: a review with emphasis on cost estimation, Ultrason. Sonochem. 17 (2010) 990–1003, https://doi.org/10.1016/j.ultsonch.2009.09.005.
[15] M. Huang, X. Wang, C. Zhu, F. Zhu, P. Liu, D. Wang, G. Fang, N. Chen, S. Gao, D. Zhou, Efficient chlorinated alkanes degradation in soil by combining alkali hydrolysis with thermally activated persulfate, J. Hazard. Mater. 438 (2022) 129571, https://doi.org/10.1016/j.jhazmat.2022.129571.
[16] T. Yu, H. Chen, T. Hu, J. Feng, W. Xing, L. Tang, W. Tang, Recent advances in the applications of encapsulated transition-metal nanoparticles in advanced oxidation processes for degradation of organic pollutants: a critical review, Appl Catal B 342 (2024) 123401, https://doi.org/10.1016/j.apcatb.2023.123401.
[17] J.C. Serna-Carrizales, A.I. Zárate Guzmán, A. Forgionny, N. Acelas, S. Pérez, J. Muñoz-Saldaña, R. Ocampo-Perez, Production of activated carbon from agave residues and its synergistic application in a hybrid adsorption-AOPs system for effective removal of sulfamethazine from aqueous solutions, Environmental Research 250 (2024) 118559, https://doi.org/10.1016/j.envres.2024.118559.
[18] Y. Li, J. Wei, N. Cui, J. Li, W. Ji, L. Wang, J. Huo, W. Yan, X. Zhang, Y. Zhao, J. Li, Atomically dispersed Fe-N_5 sites with optimized electronic structure for sustainable wastewater purification via efficient Fenton-like catalysis, Applied Catalysis b: Environment and Energy 358 (2024) 124385, https://doi.org/10.1016/j.apcatb.2024.124385.
[19] S. Liu, S. Liu, W. Wang, C. Zhang, L. Wang, Y. Liang, J. Fu, Q. Zhou, Mn-periodate complex in situ formed at Mn-N coordinate site in Mn-doped g-C_3N_5 for efficient and rapid water purification, Chem. Eng. J. 498 (2024) 155546, https://doi.org/10.1016/j.cej.2024.155546.
[20] Y. Long, S. Huang, S. Zhao, G. Xiao, J. Sun, D. Peng, Pyrolyzed iron–nitrogen–carbon hybrids for efficient contaminant decomposition via periodate activation: active site and degradation mechanism, Sep. Purif. Technol. 317 (2023) 123945, https://doi.org/10.1016/j.seppur.2023.123945.
[21] X. Yang, X. Tian, Y. Xue, C. Wang, Application of iron-modified biochar in the fields of adsorption and degradation of antibiotics, J. Environ. Manage. 380 (2025) 124875, https://doi.org/10.1016/j.jenvman.2025.124875.
[22] W. Jiang, Y. Cai, D. Liu, X. Yu, Q. Wang, Enhanced adsorption performance of oxytetracycline in aqueous solutions by Mg-Fe modified suaeda-based magnetic biochar, Environ. Res. 241 (2024) 117662, https://doi.org/10.1016/j.envres.2023.117662.
[23] L. Chen, Y. Yang, W. Tang, H. Huang, Pyrolysis of nitrilotriacetic acid-Mn/Fe to produce $MnFe_2O_4$/C nanoparticles: Excellent performance of activating periodate to degrade organic pollutants, Process Saf. Environ. Prot. 193 (2025) 239–250, https://doi.org/10.1016/j.psep.2024.11.030.
[24] W. Xiao, A. Chen, M. Cheng, W. Xiong, Y. Liu, J. Wang, G. Wang, G. Zhang, L. Li, H. Liu, Q. Shi, Mechanism insights into metal-organic framework-derived carbon materials activating periodate for p-chlorophenol removal: the role of S and Fe co-doping, Water Res. 268 (2025) 122735, https://doi.org/10.1016/j.watres.2024.122735.
[25] Y. Guo, Z. Guo, J. Wei, J. Zhang, Y. Huang, T. Hao, C. Wang, D. Xu, Iron anchored carbon–nitrogen catalyst for enhanced activation performance of peroxymonosulfate: Synergy of $^1O_2$ and high-valent iron, Sep. Purif. Technol. 353 (2025) 128381, https://doi.org/10.1016/j.seppur.2024.128381.
[26] J. Zhang, X. Li, J. Zheng, Z. Hu, J. Song, W. Hu, T. Qi, Z. Zhang, Photo-thermal coupling catalysis boosts the degradation of 1,1,1,2-tetrafluoroethane over γ-Al_2O_3/C_3N_4 catalyst, Process Saf. Environ. Prot. 190 (2024) 1105–1113, https://doi.org/10.1016/j.psep.2024.08.010.
[27] B. Yuan, Z. Qian, X. Yang, M. Luo, X. Feng, L. Fu, W. Yang, L. Yang, J. Zhang, Y. Zhao, R. Hao, Microwave-Induced Deep Catalytic Oxidation of NO using Molecular-Sieve-Supported Oxygen-Vacancy-Enriched Fe–Mn Bimetal Oxides, Environ. Sci. Technol. 56 (2022) 10423–10432, https://doi.org/10.1021/acs.est.2c02851.
[28] N. Bombuwala Dewage, A.S. Liyanage, C.U. Pittman, D. Mohan, T. Mlsna, Fast nitrate and fluoride adsorption and magnetic separation from water on α-Fe_2O_3 and Fe_3O_4 dispersed on Douglas fir biochar, Bioresource Technology 263 (2018) 258–265, https://doi.org/10.1016/j.biortech.2018.05.001.
[29] F. Chai, K. Li, C. Song, X. Guo, Synthesis of magnetic porous Fe_3O_4/C/Cu_2O composite as an excellent photo-Fenton catalyst under neutral condition, J. Colloid Interface Sci. 475 (2016) 119–125, https://doi.org/10.1016/j.jcis.2016.04.047.
[30] Y. Yang, Y. Cui, K. Zhao, H. Sun, W. Zhang, P. Kuang, X. Ma, K. Zhu, K. Ma, Unleashing the potential of biomass-doped sludge biochar: Promotion of persulfate activation by biochar-derived dissolved organic matter, Sep. Purif. Technol. 361 (2025) 131468, https://doi.org/10.1016/j.seppur.2025.131468.
[31] K. Luo, Y. Shi, R. Huang, X. Wei, Z. Wu, P. Zhou, H. Zhang, Y. Wang, Z. Xiong, B. Lai, Activation of periodate by N-doped iron-based porous carbon for degradation of sulfisoxazole: significance of catalyst-mediated electron transfer mechanism, J. Hazard. Mater. 457 (2023) 131790, https://doi.org/10.1016/j.jhazmat.2023.131790.
[32] D.L. Costa Rodrigues, A.C. Ferreira Piazzi Fuhr, J.A. Guido, C.F. De Azevedo, A. M. Rangel, G.L. Dotto, S.Y. Alomar, F.M. Machado, Olive biomass-derived magnetic activated biochar for ciprofloxacin removal: Integrated kinetic, isotherm, thermodynamic, and spectroscopic analysis, Separation and Purification Technology 360 (2025) 131014, https://doi.org/10.1016/j.seppur.2024.131014.
[33] T. Devi, N.M. Saleh, N.H.N. Kamarudin, N.J. Roslan, R. Jalil, H.A. Hamid, Efficient adsorption of organic pollutants phthalates and bisphenol a (BPA) utilizing magnetite functionalized covalent organic frameworks (MCOFs): a promising future material for industrial applications, Ecotoxicol. Environ. Saf. 268 (2023) 115706, https://doi.org/10.1016/j.ecoenv.2023.115706.
[34] Y. Huang, T. Hu, S. Li, W. Zhou, Ferrihydrite/B, N co-doped biochar composites enhancing tetracycline degradation: the crucial role of boron incorporation in Fe (III) reduction and oxygen activation, J. Environ. Sci. 154 (2025) 252–263, https://doi.org/10.1016/j.jes.2024.07.013.
[35] T. Si, R. Yuan, Y. Qi, Y. Zhang, Y. Wang, R. Bian, X. Liu, X. Zhang, S. Joseph, L. Li, G. Pan, Enhancing soil redox dynamics: Comparative effects of Fe-modified biochar (N–Fe and S–Fe) on Fe oxide transformation and Cd immobilization, Environ. Pollut. 347 (2024) 123636, https://doi.org/10.1016/j.envpol.2024.123636.

[36] Y. Zhou, Z. Liang, J. Wen, T. Liu, J. Dong, C. Chang, X. Zheng, W. Zheng, Ternary Mg-B-S co-modified Ficus virens biochar for ultra-high adsorption of rhodamine B in lab-scale and field-scale application: Adsorption behavior and mechanisms, Ind. Crop. Prod. 194 (2023) 116310, https://doi.org/10.1016/j.indcrop.2023.116310.
[37] T. Jiang, B. Wang, M. Hassan, Green synthesis of natural limonite-modified biochar catalyst for peroxymonosulfate activation in efficient degradation carbamazepine in water, J. Environ. Chem. Eng. 13 (2025) 115522, https://doi.org/10.1016/j.jece.2025.115522.
[38] Z.-T. Dong, H. Guo, Y.-Y. Yang, L. Sui, Q. Wu, X.-G. Zhang, C.-G. Niu, M. Yan, D.-W. Huang, Z.-L. Chen, Efficient generation of Fe(IV) = O for water purification in periodate activation process: reducing Fe orbital occupation and expanding electron transfer channel, Chem. Eng. J. 502 (2024) 157977, https://doi.org/10.1016/j.cej.2024.157977.
[39] P. Ma, B. Yin, M. Wu, M. Han, L. Lv, W. Li, G. Zhang, Z. Ren, Synergistic enhancement of microbes-to-pollutants and inter-microbes electron transfer by Fe, N Modified Ordered Mesoporous Biochar in Anaerobic Digestion, Journal of Hazardous Materials 476 (2024) 135030, https://doi.org/10.1016/j.jhazmat.2024.135030.
[40] H. Xiao, Y. Wang, K. Lv, C. Zhu, X. Guan, B. Xie, X. Zou, X. Luo, Y. Zhou, N-doped biochar-Fe/Mn as a superior peroxymonosulfate activator for enhanced bisphenol a degradation, Water Res. 278 (2025) 123399, https://doi.org/10.1016/j.watres.2025.123399.
[41] X. Zhu, L. Xu, C. Wang, Y. Qi, J. Shi, X. Jin, X. Bai, W. Yan, P. Jin, Insights into the enhanced simultaneous adsorption and catalytic removal of antibiotics by a novel Fe/B co-doped biochar, Sep. Purif. Technol. 360 (2025) 130888, https://doi.org/10.1016/j.seppur.2024.130888.
[42] Y. Chang, J. Li, J. Ma, Y. Liu, R. Xing, Y. Wang, G. Zhang, Oxygenated boron-doped carbon via polymer dehalogenation as an electrocatalyst for high-efficiency O_2 reduction to H_2O_2, Sci. China Mater. 65 (2022) 1276–1284, https://doi.org/10.1007/s40843-021-1891-2.
[43] X. Zhang, M. Kamali, R. Van Beeck, W. Hens, J. Truyen, D. Cabooter, R. Dewil, Degradation of ciprofloxacin using magnetite nanoparticle-activated periodate: Kinetic, mechanistic and toxicity evaluation, Chem. Eng. J. 478 (2023) 147323, https://doi.org/10.1016/j.cej.2023.147323.
[44] H. Li, N. Wang, H. Li, Z. Ren, W. Ma, J. Li, Y. Du, Q. Xu, Polyvinylpyrrolidone-induced size-dependent catalytic behavior of Fe sites on N-doped carbon substrate and mechanism conversion in Fenton-like oxidation reaction, Appl Catal B 341 (2024) 123323, https://doi.org/10.1016/j.apcatb.2023.123323.
[45] L. He, C. Yang, J. Ding, M.-Y. Lu, C.-X. Chen, G.-Y. Wang, J.-Q. Jiang, L. Ding, G.-S. Liu, N.-Q. Ren, S.-S. Yang, Fe, N-doped carbonaceous catalyst activating periodate for micropollutant removal: significant role of electron transfer, Appl Catal B 303 (2022) 120880, https://doi.org/10.1016/j.apcatb.2021.120880.
[46] C. Xiao, X. Li, Q. Li, Y. Hu, J. Cheng, Y. Chen, Ni-doped FeC_2O_4 for efficient photo-Fenton simultaneous degradation of organic pollutants and reduction of Cr(VI): Accelerated Fe(III)/Fe(II) cycle, enhanced stability and mechanism insight, J. Clean. Prod. 340 (2022) 130775, https://doi.org/10.1016/j.jclepro.2022.130775.
[47] L. Yang, Z. Xiong, J. Li, Z. Wu, X. Zhao, C. Zhao, Y. Zhou, Y. Qian, B. Lai, Iron active sites encapsulated in N-doped graphite for efficiently selective degradation of emerging contaminants via peroxymonosulfate (PMS) activation: Inherent roles of adsorption and electron-transfer dominated nonradical mechanisms, Chem. Eng. J. 444 (2022) 136623, https://doi.org/10.1016/j.cej.2022.136623.
[48] L. He, L. Lv, S.C. Pillai, H. Wang, J. Xue, Y. Ma, Y. Liu, Y. Chen, L. Wu, Z. Zhang, L. Yang, Efficient degradation of diclofenac sodium by periodate activation using Fe/Cu bimetallic modified sewage sludge biochar/UV system, Sci. Total Environ. 783 (2021) 146974, https://doi.org/10.1016/j.scitotenv.2021.146974.
[49] Y. Wang, Y. Lin, C. Yang, S. Wu, X. Fu, X. Li, Calcination temperature regulates non-radical pathways of peroxymonosulfate activation via carbon catalysts doped by iron and nitrogen, Chem. Eng. J. 451 (2023) 138468, https://doi.org/10.1016/j.cej.2022.138468.
[50] S. Wang, J. Wang, Nitrogen doping sludge-derived biochar to activate peroxymonosulfate for degradation of sulfamethoxazole: Modulation of degradation mechanism by calcination temperature, J. Hazard. Mater. 418 (2021) 126309, https://doi.org/10.1016/j.jhazmat.2021.126309.
[51] J. Yu, W. Qiu, X. Lin, Y. Wang, X. Lu, Y. Yu, H. Gu, S. Heng, H. Zhang, J. Ma, Periodate activation with stable $MgMn_2O_4$ spinel for bisphenol a removal: Radical and non-radical pathways, Chem. Eng. J. 459 (2023) 141574, https://doi.org/10.1016/j.cej.2023.141574.
[52] Q. Wang, H. Zeng, Y. Liang, Y. Cao, Y. Xiao, J. Ma, Degradation of bisphenol AF in water by periodate activation with FeS (mackinawite) and the role of sulfur species in the generation of sulfate radicals, Chem. Eng. J. 407 (2021) 126738, https://doi.org/10.1016/j.cej.2020.126738.
[53] J. Du, G. Xiao, Y. Xi, X. Zhu, F. Su, S.H. Kim, Periodate activation with manganese oxides for sulfanilamide degradation, Water Res. 169 (2020) 115278, https://doi.org/10.1016/j.watres.2019.115278.
[54] J. Sheng, S. Guo, C. Yuan, X. Nie, P. Cui, H. Jiang, Degradation bensulfuron-methyl by magnetic CoFe alloy@N-doped graphitized carbon derived from $CoFe_2O_4$ activated by peroxymonosulfate, Chem. Eng. J. 466 (2023) 143158, https://doi.org/10.1016/j.cej.2023.143158.
[55] Y. Chen, X. Duan, C. Zhang, S. Wang, N. Ren, S.-H. Ho, Graphitic biochar catalysts from anaerobic digestion sludge for nonradical degradation of micropollutants and disinfection, Chem. Eng. J. 384 (2020) 123244, https://doi.org/10.1016/j.cej.2019.123244.
[56] K.Z. Huang, H. Zhang, Direct Electron-Transfer-based Peroxymonosulfate Activation by Iron-Doped Manganese Oxide (δ-MnO_2) and the Development of Galvanic Oxidation Processes (GOPs), Environ. Sci. Technol. 53 (2019) 12610–12620, https://doi.org/10.1021/acs.est.9b03648.
[57] F. Liu, Z. Li, Q. Dong, C. Nie, S. Wang, B. Zhang, P. Han, M. Tong, Catalyst-Free Periodate Activation by Solar Irradiation for Bacterial Disinfection: Performance and Mechanisms, Environ. Sci. Technol. 56 (2022) 4413–4424, https://doi.org/10.1021/acs.est.1c08268.
[58] T. Chen, Y. Sun, H. Dong, J. Chen, Y. Yu, Z. Ao, X. Guan, Understanding the Importance of Periodate Species in the pH-dependent Degradation of Organic Contaminants in the H_2O_2/Periodate Process, Environ. Sci. Technol. 56 (2022) 10372–10380, https://doi.org/10.1021/acs.est.2c02446.
[59] E.-T. Yun, J.H. Lee, J. Kim, H.-D. Park, J. Lee, Identifying the Nonradical Mechanism in the Peroxymonosulfate Activation Process: Singlet Oxygenation Versus Mediated Electron transfer, Environ. Sci. Technol. 52 (2018) 7032–7042, https://doi.org/10.1021/acs.est.8b00959.
[60] B. Liu, W. Guo, H. Wang, Q. Si, Q. Zhao, H. Luo, N. Ren, B-doped graphitic porous biochar with enhanced surface affinity and electron transfer for efficient peroxydisulfate activation, Chem. Eng. J. 396 (2020) 125119, https://doi.org/10.1016/j.cej.2020.125119.
[61] C.-Y. Hu, Z.-Y. Dong, Z.-Y. Dong, Y.-H. Wu, S.-J. Ji, L.-L. Hu, X.-Y. Yang, H. Liu, B. Xu, Insight into the activation of periodate by Mn(II) for rapid degradation of sulfadiazine: Performance and mechanisms, Sep. Purif. Technol. 342 (2024) 127023, https://doi.org/10.1016/j.seppur.2024.127023.
[62] Y. Bu, H. Li, W. Yu, Y. Pan, L. Li, Y. Wang, L. Pu, J. Ding, G. Gao, B. Pan, Peroxydisulfate Activation and Singlet Oxygen Generation by Oxygen vacancy for Degradation of Contaminants, Environ. Sci. Technol. 55 (2021) 2110–2120, https://doi.org/10.1021/acs.est.0c07274.
[63] P. Liang, C. Zhang, X. Duan, H. Sun, S. Liu, M.O. Tade, S. Wang, An insight into metal organic framework derived N-doped graphene for the oxidative degradation of persistent contaminants: formation mechanism and generation of singlet oxygen from peroxymonosulfate, Environmental Science-Nano 4 (2017) 315–324, https://doi.org/10.1039/C6EN00633G.
[64] Y. Yao, Z. Ma, Z. Ma, S. Wang, L. Zhang, Y. Wang, S. Wang, Dual single atomic Fe-Ni sites in N-doped nanoporous carbon for high-efficiency potassium periodate activation toward pollutant abatement, Sep. Purif. Technol. 353 (2025) 128091, https://doi.org/10.1016/j.seppur.2024.128091.
[65] Y. Yu, X. Chen, L. Tao, Y. Li, L. Wu, Z. Chen, X. He, Y. Luo, L. Yang, Fe-Mn bimetallic loaded sludge biochar as a novel periodate activator for sulfamethoxazole removal: the combination of radical and non-radical mechanisms, Environ. Res. 285 (2025) 122515, https://doi.org/10.1016/j.envres.2025.122515.
[66] H. Zeng, Y. Chen, J. Xu, S. Li, J. Wu, D. Li, J. Zhang, Iron-based materials for activation of periodate in water and wastewater treatment processes: the important role of Fe species, Chem. Eng. J. 482 (2024) 148885, https://doi.org/10.1016/j.cej.2024.148885.
[67] W. Xu, X. Zheng, Z. Shangguan, J. Qu, W. Zhang, A low-cost magnetic catalyst ($MnFe_2O_4$) for ciprofloxacin degradation via periodate activation: the synergistic effect of Mn and Fe, Chem. Eng. J. 464 (2023) 142562, https://doi.org/10.1016/j.cej.2023.142562.
[68] T. Lu, Q. Chen, Independent gradient model based on Hirshfeld partition: a new method for visual study of interactions in chemical systems, J. Comput. Chem. 43 (2022) 539–555, https://doi.org/10.1002/jcc.26812.
[69] H.F. Shakir, T. Zhao, M.U. Farooq, A. Jalil, Mn-Mo ferrites doped with rare earth element for enhancing EMI shielding: a DFT calculation and experimental comparison, Journal of Materials Science & Technology 224 (2025) 183–190, https://doi.org/10.1016/j.jmst.2024.11.015.
[70] Q. Wei, P. Zhang, X. Guo, W. Jiang, X. Tao, P.K. Shen, Z.Q. Tian, Atomic spin engineering of Fe-N-C by axial chlorine-ligand modulation for lightweight and efficient electromagnetic wave absorption, J. Colloid Interface Sci. 692 (2025) 137464, https://doi.org/10.1016/j.jcis.2025.137464.
[71] P. Zhang, Q. Wei, J. Su, X. Guo, P.K. Shen, Z. Li, Z.Q. Tian, Strengthening the d-p orbital hybridization of N-doped carbon nanocages with encapsulated Fe nanoparticles for efficient electromagnetic wave absorption, Chem. Eng. J. (2025) 163716, https://doi.org/10.1016/j.cej.2025.163716.
[72] J. Liu, J. Zhu, Q. Gao, X. Zeng, Q. Zeng, J. Xiong, G. Zhang, Y. Niu, H. Xie, Accelerate degradation of tetracycline via persulfate activation over S,N-Fe co-doped banana peel biochar: the role of pyrolysis temperature and $^1O_2$ evolution, Chem. Eng. J. 509 (2025) 161425, https://doi.org/10.1016/j.cej.2025.161425.
[73] Y. Yang, Z. Kang, G. Xu, Y. Yu, Nitrogen and magnesium codoped biochar activates periodate to remediate bensulfuron methyl-contaminated water at low temperature: Performance, mechanisms, and phytotoxicity, J. Hazard. Mater. 480 (2024) 135803, https://doi.org/10.1016/j.jhazmat.2024.135803.
[74] X.-J. Chen, C.-W. Bai, Y.-J. Sun, X.-T. Huang, B.-B. Zhang, Y.-S. Zhang, Q. Yang, J.-H. Wu, F. Chen, pH-driven Efficacy of the Ferrate(VI)–Peracetic Acid System in Swift Sulfonamide Antibiotic Degradation: a Deep Dive into active Species Evolution and Mechanistic Insights, Environ. Sci. Technol. 57 (2023) 20206–20218, https://doi.org/10.1021/acs.est.3c06370.
[75] S. Liu, S. Liu, T. Wang, L. Yang, L. Li, X. Wu, Z. Si, R. Ran, H. Wu, Visible light assisted periodate activation with porous C_3N_5 for tetracycline degradation: Enhanced electron-hole separation and reactive oxygen species formation, Chem. Eng. J. 498 (2024) 155739, https://doi.org/10.1016/j.cej.2024.155739.
[76] C. Zhu, F. Cun, Z. Fan, Y. Nie, Q. Du, F. Liu, W. Yang, A. Li, Heterogeneous Fe-Co dual-atom catalyst outdistances the homogeneous counterpart for peroxymonosulfate-assisted water decontamination: New surface collision oxidation path and diatomic synergy, Water Res. 241 (2023) 120164, https://doi.org/10.1016/j.watres.2023.120164.

[77] D. Chen, C. Ma, Q. Zhang, C. Xue, H. Che, Y. Ao, Construction of bifunctional S-doped N-deficient carbon nitride for efficient simultaneous photocatalytic H_2O_2 synthesis and BPA degradation, Surf. Interfaces 52 (2024) 104886, https://doi.org/10.1016/j.surfin.2024.104886.

[78] X. Lv, A. Shu, L. Shu, H. Liu, Y. Liu, K. Cui, Y. Tang, X. Chen, Electron cycling mechanism in Fe/Mn DSAzyme accelerates BPA degradation and nanoenzyme regeneration, J. Hazard. Mater. 476 (2024) 135228, https://doi.org/10.1016/j.jhazmat.2024.135228.

[79] P. Wang, Y. Zhang, J. Zhu, J. Wei, J. Qi, T. Cao, M. Yang, Catalytic degradation of BPA by bamboo leaf-derived KOH-activated porous biocarbon loaded with $CoFe_2O_4$-activated peroxymonosulfate, Chem. Eng. J. 492 (2024) 151886, https://doi.org/10.1016/j.cej.2024.151886.

[80] H. Zhang, C.-H. Huang, Reactivity and Transformation of Antibacterial *N* -Oxides in the Presence of Manganese Oxide, Environ. Sci. Technol. 39 (2005) 593–601, https://doi.org/10.1021/es048753z.

[81] P. Xu, N. Li, J. Ma, J. Yao, B. Hou, Performance and mechanism of tetracycline degradation by $CuCo_2O_4$ nanomaterial activated periodate, Environ. Pollut. 378 (2025) 126506, https://doi.org/10.1016/j.envpol.2025.126506.

[82] L. Qin, S. Hu, H. Yi, W. Wang, C. Lai, S. Liu, D. Ma, T. Tong, H. Deng, G. Lv, B-doped lotus pollen biochar photothermal activating periodate for acetaminophen degradation by non-radical pathway: significance of thermal effect from the photothermal process, Sep. Purif. Technol. 375 (2025) 133707, https://doi.org/10.1016/j.seppur.2025.133707.